Spatial Characterization of Bioenergetics and Metabolism of Primordial to Preovulatory Follicles in Whole Ex Vivo Murine Ovary[1]

Rachel Cinco,[3] Michelle A. Digman,[4,5] Enrico Gratton,[4,5] and Ulrike Luderer[2,3,6,7]

[3]Department of Developmental and Cell Biology, University of California Irvine, Irvine, California
[4]Laboratory for Fluorescence Dynamics, University of California Irvine, Irvine, California
[5]Department of Biomedical Engineering, University of California Irvine, Irvine, California
[6]Department of Medicine, University of California Irvine, Irvine, California
[7]Program in Public Health, University of California Irvine, Irvine, California

ABSTRACT

Previous work characterizing ovarian bioenergetics has defined follicular metabolism by measuring metabolic by-products in culture media. However, culture conditions perturb the native state of the follicle, and these methods do not distinguish between metabolism occurring within oocytes or granulosa cells. We applied the phasor approach to fluorescence lifetime imaging microscopy (phasor FLIM) at 740-nm two-photon excitation to examine the spatial distribution of free and protein-bound nicotinamide adenine dinucleotide hydride (NADH) during primordial through preovulatory stages of follicular development in fresh ex vivo murine neonatal and gonadotropin stimulated prepubertal ovaries. We obtained subcellular resolution phasor FLIM images of primordial through primary follicles and quantified the free/bound NADH ratio (relative NADH/NAD+) separately for oocyte nucleus and oocyte cytoplasm. We found that dynamic changes in oocyte nucleus free/bound NADH paralleled the developmental maturation of primordial to primary follicles. Immunohistochemistry of NAD+-dependent deacetylase SIRTUIN 1 (SIRT1) in neonatal ovary revealed that increasing SIRT1 expression in oocyte nuclei was inversely related to decreasing free/bound NADH during the primordial to primary follicle transition. We characterized oocyte metabolism at these early stages to be NADH producing (glycolysis/Krebs). We extended the results of prior studies to show that cumulus and mural granulosa cell metabolism in secondary through preovulatory follicles is mainly NADH producing (glycolysis/Krebs cycle), while oocyte metabolism is mainly NADH consuming (oxidative phosphorylation). Taken together, our data characterize dynamic changes in free/bound NADH and SIRT1 expression during early follicular development and confirm results from previous studies defining antral and preovulatory follicle metabolism in culture.

cumulus cells, FLIM, folliculogenesis, glycolysis, granulosa cells, Krebs cycle, NADH, oocyte, oxidative phosphorylation, phasor approach to fluorescence lifetime imaging microscopy, sirtuin 1

INTRODUCTION

The ovarian follicle consists of a single oocyte encapsulated within somatic granulosa cells. The ovarian follicular reserve is maintained as a pool of quiescent primordial follicles. Over time, small cohorts of quiescent primordial follicles become activated into the growing pool and mature through transitional, primary, secondary, antral, and preovulatory stages of development. The transition rate of quiescent primordial follicles into activated transitional follicles is a critical process in determining the rate at which the ovarian reserve and fertile life span are exhausted. Early exhaustion of the primordial follicle pool from primordial follicle hyperactivation causes premature ovarian failure in several mouse models [1]. However, the molecular mechanisms that underlie the balance between follicular quiescence and activation during this critical period are not fully defined.

Follicular bioenergetics are critical determinants of oocyte quality and ovarian aging [2]. Most studies of ovarian bioenergetics have defined follicular metabolism by measuring glucose, lactate, and pyruvate concentrations in culture media. These studies have concluded that whole follicles follow a metabolic trajectory toward increased glycolysis as they progress from secondary to preovulatory stages [3–6]. However, culture conditions perturb redox status, signaling pathways, and epigenetics [7–10]. Moreover, the majority of follicular bioenergetics studies focused on secondary through later stage follicles [3, 11–13], with few studies examining bioenergetics in primordial or transitional follicles [14]. These forms of analysis are also incapable of defining metabolism in single cells or in subfollicular compartments within the intact ovary.

Nicotinamide adenine dinucleotide (NAD) and its reduced form NADH play a central role in bioenergetics as a main energy cofactor in the cell. NADH is ubiquitous in cells and plays critical roles as an enzymatic cofactor and reducing equivalent in cellular metabolic and redox reactions. The NADH/NAD+ ratio has a significant impact on energy production, cell survival, proliferation, longevity, and aging [15, 16].

NADH is naturally autofluorescent, and previous studies have established that fluorescence measurements of free and bound forms of NADH can be utilized to deduce cellular metabolism [17–21]. Glycolysis and the Krebs cycle are major

NADH-producing pathways, and oxidative phosphorylation is a major NADH-consuming pathway. During glycolysis/Krebs cycle metabolism, high levels of NADH are produced and maintained. However, during oxidative phosphorylation, NADH is consumed, lowering the levels of available NADH. Decreased availability of NADH lowers substrate concentrations and correspondingly shifts enzyme kinetics toward increased bound NADH [22]. Based on this principle, the free/bound NADH has been used to infer the ratio of NADH-producing glycolysis/β-oxidation/Krebs metabolism to NADH-consuming oxidative phosphorylation [17–21, 23].

SIRT1 is a key NAD+-dependent deacetylase, which is regulated by nuclear levels of NADH [24–26]. SIRT1 expression has been reported in rat and mouse ovaries [27, 28]. SIRT1 deacetylates the transcription factor FOXO3a [29], which is an important regulator of primordial follicle activation [30, 31]. SIRT1 also deacetylates PGC-1α, which is involved in mitochondrial biogenesis and glucose/fatty acid metabolism [32, 33]. However, SIRT1 expression during the early stages of follicle development has not been defined.

The development of the phasor approach to fluorescence lifetime imaging microscopy (phasor FLIM) provides a straightforward approach to interpretation of lifetime differences at the pixel level [34]. Phasor FLIM using 740-nm two-photon excitation has been extensively used to characterize the spatial distribution of the free/bound NADH ratio in living cells and tissues [17, 35–38]. The fluorescence lifetime of free NADH is 0.4 ns, while the average fluorescence lifetime of bound NADH is approximately 3.4 ns [17, 36, 39]. This large difference is easily recognized in the phasor plot [35]. The phasor FLIM analysis of an image provides a quantitative measure of the ratio of free/bound NADH, which mimics the ratio of intracellular NADH/NAD+ [17, 20, 23], with the added advantage of visualizing and quantifying the spatial distribution of free and bound NADH pixels within an image and within regions of interest.

Quiescent and newly activated small follicles constitute the majority of follicles in a fertile ovary; however, the bioenergetics of ovarian follicles at these stages are poorly characterized. In the present study, we used phasor FLIM to quantify the free/bound NADH ratio separately for oocyte and granulosa cell subcompartments within individual follicles inside whole ovarian tissue at primordial through preovulatory stages of folliculogenesis. Furthermore, we assessed follicle free/bound NADH changes in response to glycolysis and oxidative phosphorylation inhibitors to clarify contributions of each metabolic pathway to overall NADH production.

MATERIALS AND METHODS

Animals

Male and female C57BL/6J (bred in our colony from mice originally obtained from Jackson Laboratories) were mated to generate postnatal day (PND) 4–10 or PND 23 female offspring for analyses. Heterozygous TgOG2 strain mice expressing GFP under a modified germ-line-specific Oct-4 promoter [40] were bred by crossing male homozygous breeders obtained from the Jackson Laboratories with C57BL/6J female mice. Mice were housed in an American Association for the Accreditation of Laboratory Animal Care-accredited facility and maintained on a 14L:10D schedule with free access to soy-free rodent chow (Harlan Teklad 2019) and deionized water. Temperature was maintained at 21°C–23°C. Female mice were euthanized on PND 4–6 or PND 25–26 for phasor analysis and PND 7–10 for immunohistochemistry. Neonatal mice were euthanized by decapitation followed by incision of the diaphragm. Older mice were euthanized by cervical dislocation immediately followed by incision of the diaphragm. Ovaries were dissected and bursa removed in Hanks Balanced Salt Solution (HBSS) supplemented with calcium and magnesium at 37°C (Invitrogen 14025-092). All animal procedures were performed with adherence to NIH OLAW and were approved by the Institutional Animal Care and Use Committee at the University of California, Irvine.

Genotyping of GFP-expressing TgOG2 mice was performed on DNA extracted by HOTSHOT DNA extraction [41] using tail snips that were incubated with 50 mM NaOH at 98°C for 1 h, then quenched with 1 M Tris-HCl. PCR was then carried out using primers designed for detection of an X-linked GFP transgene with the following primer sequence: X-GFP-F: 5′-ATCTTCTTCAAGGACGACGGCAAC-3′, X-GFP-R: 5′-TCCTCGATGTTG TGGCGGATCTTG-3′.

Sample Preparation

Ovaries were dissected and submerged between two glass coverslips separated by 2-mm spacers in 500 μl 1% low-melt agarose (SeaPlaque, Lonza) in HBSS (Invitrogen 14025-092) heated to 37°C. The stock HBSS and 1% low-melt agarose was equilibrated with air and was therefore oxygenated, providing an oxygen source for the ovary during the duration of imaging. We compared signal intensity, lifetime, and quality of images taken at the beginning versus the end of an imaging session from the same ovary and observed no changes over a 1.5-h period.

Stimulation of Prepubertal Females to Promote Antral and Preovulatory Follicle Growth

PND 23 females were intraperitoneally injected with 5 IU equine chorionic gonadotropin (eCG; National Hormone and Peptide Program, Los Angeles Biomedical Research Institute) at 1400 h. Some females were euthanized 48 h post-eCG, and whole ovaries were imaged for secondary, antral, or preovulatory stage follicles (these are designated eCG follicles in figures). Other females were intraperitoneally injected 46 h after eCG with 5 IU human chorionic gonadotropin (hCG; Sigma CG10) and euthanized 7–9 h later for imaging of secondary, antral, and preovulatory follicles (these are designated eCG+hCG follicles).

Imaging

PND 4–9 ovaries were embedded between two cover glasses separated by 0.2-mm-thick spacers in 1% low-melt agarose in HBSS heated to 37°C and immediately imaged by FLIM using the DIVER microscope at the Laboratory for Fluorescence Dynamics at the University of California, Irvine. The DIVER is an Olympus upright microscope coupled to a two-photon excitation Spectra-Physics MaiTai HP/ Insight DS+, DeepSee laser, and large area PMT detector [42, 43] operating in nondescanned mode using FlimBox devices and controlled by SimFCS software developed at the Laboratory for Fluorescence Dynamics [44]. Detection of follicles in whole ovary was performed using the intensity imprint apparent from live acquisition of autofluorescent NADH excited at 740 nm using a 63× 1.25 NA oil Zeiss objective lens and paired with a Kopp Blue #5543 filter (Greyglass) that blocks light outside of ~350–510 nm. Approximately ≤4-mW laser power was applied to the sample, determined through power meter measurements after the objective lens. The live acquisition of NADH autofluorescence at 740-nm two-photon yields a clear intensity imprint that allows for morphometric identification of follicles in the field of view, which we utilized for follicle staging and identification. GFP-labeled oocytes from whole PND4 TgOG2 ovary were visualized using 880-nm two-photon excitation paired with a 500-nm long-pass filter that restricts wavelengths below 500 nm (Edmund Optics #66-050). FLIM calibration was performed using the known fluorescence lifetime of Rhodamine 110 exhibiting a single exponential decay of approximately 4 ns [45]. All FLIM imaging acquisition was limited to 1.5 h after animal sacrifice. FLIM images uniformly consisted of a size of 256 × 256 pixels, scanned at a speed of 32 μsec/pixel. Ten frames per field of view were acquired for GFP fluorescence, whereas 50 frames per field of view were recorded for NADH fluorescence. We verified that the direct excitation of GFP in the tissue at 740 nm (used for NADH excitation) was minimal. To further increase the separation between the two fluorescent species, the Kopp Blue filter selected for only the emission of NADH.

PND 23 ovaries were embedded between two cover glasses separated by spacers and imaged using a 40× 0.8 NA water immersion Olympus objective lens paired with the same microscope and filters as above.

Morphometric Staging Rubric

Primordial follicles were defined as having exclusively flat granulosa cells, transitional follicles as having a combination of flat and cuboidal granulosa cells, primary follicles as having 10 or more exclusively cuboidal granulosa cells in a single cross section, secondary follicles as having more than one layer

of granulosa cells, and antral follicles as having an antral cavity [46, 47]. Morphometric analysis took account of both intensity and FLIM images for accuracy.

FLIM Analysis and Quantification of the Average Phasors per Region of Interest

All FLIM analysis was performed using Globals for Images software (SimFCS) [44], based on previously established methods [17, 35, 37, 38]. Visual interpretation of the spatial enrichment of free and bound forms of NADH within the phasor FLIM images was facilitated by the color bar code depicted in the 740-nm phasor FLIM histogram (Fig. 1, A and B), where red pixels in the phasor FLIM image represent regions of more free NADH and light blue to yellow pixels represent more bound NADH based on cursor placement within the phasor FLIM 2D histogram in the SimFCS software (Fig. 1C, lower histogram). Control and treatment group images were subjected to identical cursor placement, where cursor placement was defined to cover the 2D histogram distribution spread of all control images (cursor placement example is shown in Fig, 1B). Color changes in the treatment group represent changes relative to all control images for every experiment.

Quantification of the average NADH phasor per region of interest was calculated using the built-in masking feature in SimFCS. This masking feature averages the lifetime of all pixels included within a designated region of interest. Image segmentation was done by using free-form shapes manually drawn around the following regions of interest: oocyte nuclei and oocyte cytoplasm across multiple follicles of different developmental stages based on morphometric analysis of both intensity and FLIM painting images for accurate boundary placement. For imaging of secondary and antral follicles in PND 25–26 ovaries, we masked 1) the oocyte cytoplasm (image cross-sections containing the oocyte nucleus were rare, and therefore oocyte nuclei were not analyzed), 2) the ring of granulosa cells directly surrounding the oocyte as cumulus granulosa cells, and 3) the outer frame of granulosa cells that border the follicular diameter inside the enclosure of bright-intensity/high-bound NADH theca cells as mural granulosa cells. Minimal histogram thresholding to remove low-intensity pixels was applied to improve visualization in reference follicle images used only to clarify follicle structures. Quantitation of the average NADH phasor lifetime within each mask was calculated from unaltered, unthresholded FLIM data and output in terms of G and S values, where $G = m \cdot \cos (\Phi)$ and $S = m \cdot \sin (\Phi)$ [35]. Transformation of G and S into the free/bound ratio of NADH was accomplished by transforming average phasor G and S coordinates into lifetime, τ [35], followed by calculation of the distance of average τ to the τ of free NADH ($\tau = 0.4$ ns) divided by the distance of the average τ to the τ of bound NADH ($\tau = 3.4$ ns) on the universal circle.

Glycolysis and Oxidative Phosphorylation Inhibition Experiments

For glycolysis inhibition, PND 4–5 ovaries were cultured on floating membranes in DMEM/F12 media without pyruvate (Gibco Life Technologies #ME16043L1). Ovaries were treated with or without 25 mM or 50 mM 2-deoxyglucose (2-DG, Sigma-Aldrich #D8375) for 15 h prior to imaging to inhibit conversion of glucose to glucose-6-phosphate in tissue (Supplemental Figure S1; all Supplemental Data are available online at www.biolreprod.org). We chose these concentrations based on desired competition (1.5× or 3×) with the concentration of glucose (17 mM) in DMEM/F12 media. Additional ovaries were cultured with or without 100 mM sodium dichloroacetate (Na DCA), a pyruvate mimetic [48] (Sigma-Aldrich #347795), for 6 or 15 h prior to imaging (Supplemental Figure S1). For oxidative phosphorylation inhibition (Supplemental Figure S1), PND 4–5 ovaries were cultured on floating membranes in DMEM/F12 media (Gibco Life Technologies #11320033) overnight prior to addition of a small volume of 1 M potassium cyanide (KCN) (Sigma-Aldrich #60178) stock solution dissolved in media. Final concentration of KCN applied to treated ovaries was 1 mM [49, 50] or 4 mM KCN [17, 38] for a span of 1 h prior to imaging. The same 1 M KCN stock solution was added to HeLa cell controls for a final concentration of 1 mM KCN incubated for 10 min prior to imaging.

Immunohistochemistry

Ovaries fixed in Bouins fluid (Electron Microscopy Sciences #15990) were cryosectioned at 8 μm. Sections were subjected to 20 min of antigen retrieval in 10 mM sodium citrate, 15 min of avidin/biotin block (Vector Laboratories SP-2001), and 1 h of blocking in 5% goat serum prior to staining with a 1:2000 dilution of rabbit polyclonal anti-SIRT1 (Sir2) antibody (Millipore #07-131) overnight. Slides were then washed three times with PBST and incubated with Vectastain ABC (Vector Laboratories PK-4001) prior to 5 min of incubation

with 3,3′-diaminobenzidine substrate in peroxide buffer (Roche) and counterstaining with hematoxylin. Positive control brain tissue demonstrated immunostaining in previously defined SIRT1-positive brain regions, such as the hippocampus [51]. Negative controls with nonimmune IgG replacing the primary antibody or with primary antibody without secondary antibody showed no staining.

Statistical Analysis

Data were analyzed using generalized estimating equations (GEE), a form of generalized linear model, to adjust for multiple follicles being evaluated from the same animal. In these analyses, the animal was included as a subject variable. The working correlation matrix structure was set as unstructured unless the unstructured matrix did not converge, in which case an exchangeable structure was used. Estimated marginal means and standard errors from the GEE models are reported in the graphs. Analyses were performed using SPSS version 23 for Macintosh (IBM Corporation).

RESULTS

Subcellular Resolution of Follicular Morphology in 740-nm Two-Photon Excitation Intensity Images

The spatial distribution of NADH excited at 740 nm outlined follicle regions of interest in the NADH intensity images, enabling us to delineate oocyte nuclei, oocyte cytoplasm, and granulosa cell nuclei (Figs. 1A and 2A). To verify that visualized follicle outlines from acquired NADH intensity images were genuine follicles, we imaged PND 4–5 ovaries with oocyte-specific GFP expression under control of a modified Oct4 promoter [40]. GFP oocytes overlapped with structures identified as oocytes of follicles in NADH intensity imprints, authenticating these structures as genuine follicles (Fig. 1A).

Discernible follicle outlines from the NADH intensity images facilitated the identification of granulosa cell morphology. This allowed us to categorize follicles using a classic morphometric staging rubric. Figure 1A depicts neighboring primordial follicles distinguished by exclusively flat granulosa cells.

Oocyte Nuclei of Primordial Follicles Have Higher Free/Bound NADH Ratios Than Primary Follicles

To observe the dynamic changes in free/bound NADH during early stages of folliculogenesis, we imaged whole live PND 4–9 ovaries, which are enriched for primordial to primary follicle stages. Comparison of primordial, transitional, and primary follicle images collected from whole neonatal ovaries revealed obvious changes in spatial dynamics of NADH intensity and free/bound NADH ratio (Fig. 2A). Visual examination of intensity images revealed two populations of primordial follicles: those with even NADH intensity throughout the cytoplasm and nucleus (Fig. 2A, upper row, middle image primordial follicles) and those with low NADH intensity in the nucleus (Fig. 2A, upper row, right image primordial follicles). NADH intensity was also low in transitional and primary oocyte nuclei (Fig. 2A, upper row). Examination of FLIM images (Fig. 2A, lower row) revealed increased bound NADH (blue pixels) in oocyte nuclei during primordial to primary follicle progression.

The free/bound FLIM image of the oocyte cytoplasm at all stages appears enriched for red pixels (high free/bound ratio, more free NADH), suggesting that metabolism at these stages has strong contributions from NADH-producing pathways, such as glycolysis and the Krebs cycle (Fig. 2A). To quantify the developmental changes in free/bound NADH across follicle stages, we masked individual regions of interest corresponding to the oocyte nucleus and oocyte cytoplasm. We displayed this
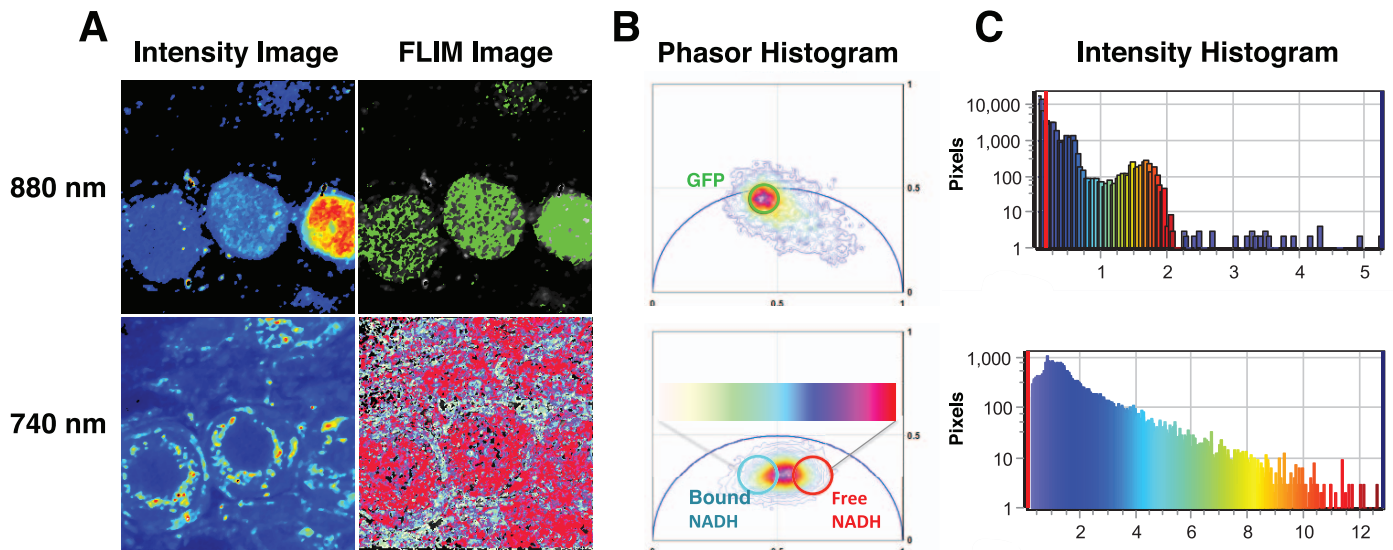
FIG. 1. Apparent oocytes in 740-nm two-photon excitation intensity images colocalize with oocyte-specific GFP fluorescence. **A**) Intensity (left) and FLIM images (right) of TGOG2 mouse ovaries with germ-line-specific GFP expression; 880-nm two-photon excitation specific for GFP and 740-nm two-photon excitation specific for NADH; 58-μm field of view. **B**) Phasor FLIM lifetime pixel distribution of corresponding images represented in 2D histograms. Color bar on the 740-nm NADH phasor 2D histogram represents the color code of free/bound NADH in the FLIM image. **C**) Intensity histogram of image pixels for GFP at 880-nm two-photon excitation (upper) and NADH at 740-nm two-photon excitation (lower), where X-axis is intensity and Y-axis is pixels. A low-level threshold (red vertical line on left of histogram) was applied to 880-nm GFP images to eliminate background, and no threshold was applied to 740-nm NADH images.

information in the form of g versus s plots (Figs. 2, C and E) and transformed average free/bound NADH bar graphs that were used for statistical analysis (Figs. 2, B and D; refer to *Materials and Methods*). Comparisons among primordial, transitional, and primary follicle stages revealed significant changes in oocyte nuclear free/bound NADH (Fig. 2, A and B). Primordial follicle oocyte nuclei showed significantly higher ratios of free/bound NADH compared to transitional and primary follicles (N = 22 follicles across nine animals, effect of follicle type, $P < 0.001$; Fig. 2B). Differences among oocyte cytoplasmic free/bound NADH ratios varied less across follicle stages; primordial follicles had the highest ratio, but intergroup comparisons were statistically significant only for primordial compared to transitional follicles ($P = 0.020$, effect of follicle stage; Fig. 2D).

Glycolysis Inhibition with 2-DG and Na DCA Decreases Free/Bound NADH

Because glycolysis and the Krebs cycle are NADH producing and oxidative phosphorylation is NADH consuming, the free/bound NADH ratio may be utilized to interpret metabolism in cells. To examine the contribution of NADH-producing metabolic pathways in oocytes of early stage follicles, we cultured PND 4–5 ovaries with 25 or 50 mM 2-DG for 15 h. 2-DG is a competitive inhibitor of hexokinase, the metabolic enzyme involved in conversion of glucose to glucose-6-phosphate (Supplemental Figure S1). Glucose-6-phosphate is required for production of pyruvate, which is important for the Krebs cycle. Nuclei and cytoplasm of oocytes in ovaries cultured with 2-DG exhibited pronounced shifts toward more bound NADH compared to 15-h control cultures (Supplemental Figure S2, A and B), indicating that these follicles rely on glucose for NADH production and are using glycolysis for metabolism. Moreover, observed changes in free/bound NADH in response to 2-DG serve as a positive control for phasor FLIM quantitation of changes in free/bound NADH.

To specifically test oocyte dependency on pyruvate, we cultured PND 4–5 ovaries with 100 mM Na DCA, a pyruvate mimetic (Supplemental Figure S1) for 6 and 15 h. Oocytes in ovaries cultured with Na DCA exhibited pronounced nuclear and cytoplasmic shifts toward more bound NADH in FLIM images at both the 6- and the 15-h time points compared to ovaries cultured in control media (Supplemental Figure S2, C and D). Moreover, at 15 h, the observed NADH intensity decreased to the extent that it became difficult to identify follicle structures using identical laser power (Supplemental Figure S2C).

Although we did not quantify free/bound NADH in granulosa cells, our FLIM images are consistent with predominantly glycolytic metabolism in granulosa cells of these early stage follicles. We observed even more pronounced shifts toward bound NADH in granulosa and interstitial cells than in oocytes in response to 2-DG and Na DCA compared to controls in FLIM images (shift from red to blue; Supplemental Figure S2, A and C). Taken together, these data suggest that primordial to primary stage follicles are dependent on pyruvate for metabolism.

Oxidative Phosphorylation Inhibition of Neonatal Ovaries Does Not Increase Free NADH

To assess the contribution of the NADH-consuming oxidative phosphorylation in early stage follicles, we treated PND 4–5 ovaries with 1 or 4 mM KCN. KCN is an inhibitor of oxidative phosphorylation that binds directly to cytochrome c oxidase [17, 38, 52]. If cells are utilizing oxidative phosphorylation, KCN treatment should increase levels of free NADH (Supplemental Figure S1). As expected, positive control HeLa cells treated with KCN for 10 min showed the expected increase in free/bound NADH (Supplemental Figure S3A). However, treatment of PND 4–5 neonatal ovaries with 1 or 4 mM KCN for 1 h in culture resulted in significantly decreased rather than increased free/bound NADH in both nuclei and cytoplasm of oocytes (Supplemental Figure S3, B and C),
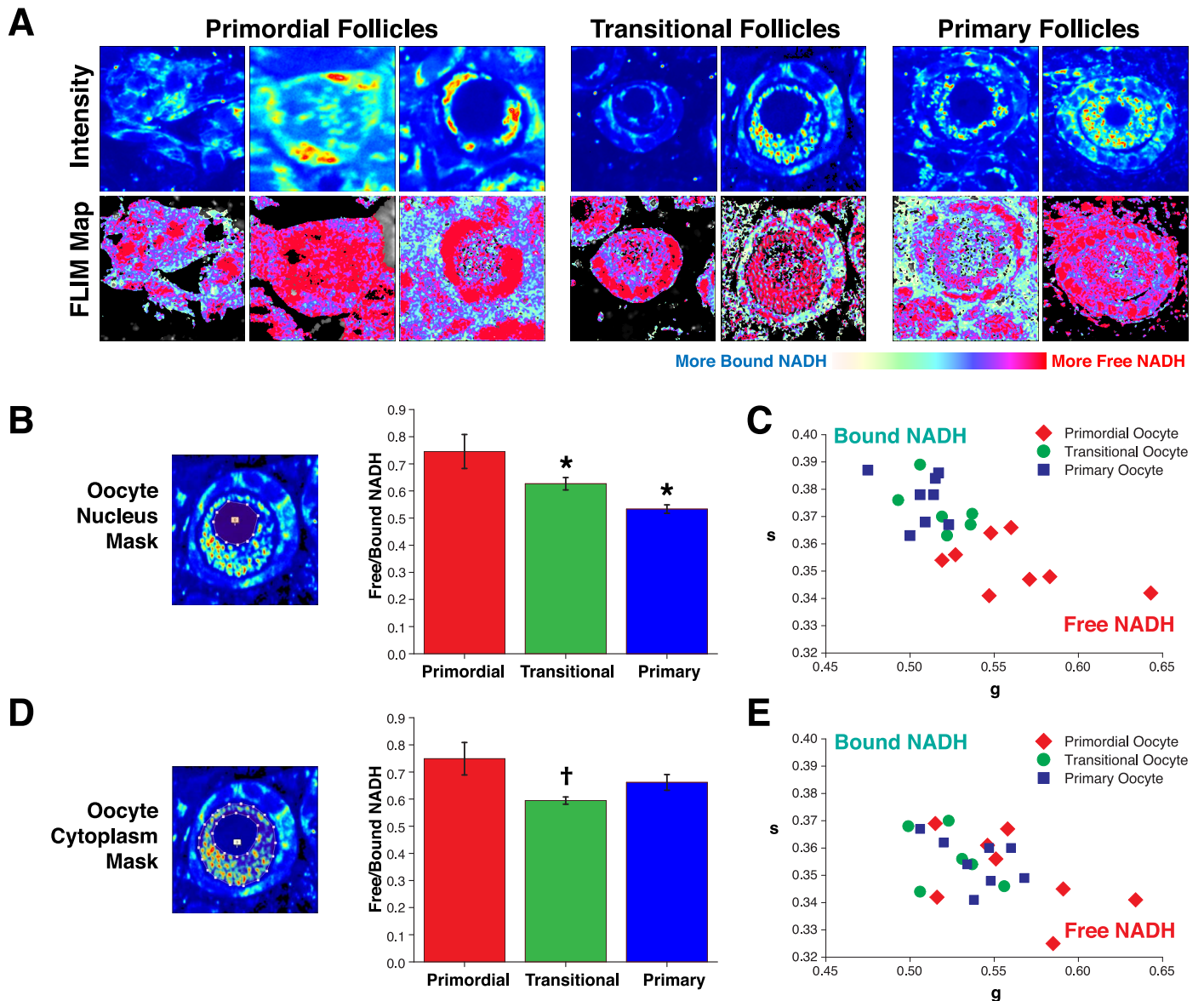
FIG. 2. Spatial NADH intensity and lifetime dynamics over the course of early stages of folliculogenesis. **A**) 740-nm two-photon excitation intensity images and lifetime FLIM images of primordial follicles, transitional follicles, and primary follicles imaged within PND 4–7 neonatal ovary. Minimal threshold applied to FLIM map reference images to highlight only follicle structures. Field of view from left to right: 60 μm, 30 μm, 38 μm, 38 μm, 46 μm, 60 μm, and 90 μm. **B**) Depiction of oocyte nucleus mask applied to unaltered/unthresholded images to quantify average free/bound NADH pixels per oocyte nucleus and resulting quantitation of mean ± SEM free/bound NADH for primordial, transitional, and primary follicle nuclei ($P < 0.001$, effect of follicle type by GEE; $*P < 0.05$ vs. primordial) transformed from C. **C**) Average free/bound NADH pixels per oocyte nucleus plotted as g versus s along the free/bound NADH axis; N = 22 follicles across nine animals. **D**) Depiction of oocyte cytoplasm mask applied to quantify average free/bound NADH and resulting mean ± SEM free/bound NADH pixels for primordial, transitional, and primary follicle cytoplasm ($P = 0.020$, effect of follicle type by GEE; $†P < 0.05$ vs. primary) transformed from E. **E**) Average free/bound NADH per oocyte cytoplasm plotted as g versus s along the free/bound NADH axis; N = 22 follicles across seven animals.

consistent with minimal contribution of oxidative phosphorylation to follicular metabolism at these stages.

Changes in SIRT1 Protein Expression Are Inversely Related to Nuclear NADH

To further understand the increases in bound NADH we observed in oocyte nuclei over the course of primordial to transitional/primary stages of folliculogenesis, we examined the expression of a prominent NAD+-dependent deacetylase, SIRT1. Immunostaining of PND 7–9 ovaries with anti-SIRT1 revealed that a subset of primordial follicles, which were localized in the ovarian medulla, had immunopositive nuclei

(Fig. 3, A and C), whereas primordial follicles immunonegative for SIRT1 were localized in the cortex (Fig. 3, A and B). In contrast, all transitional and primary staged follicles were immunopositive for SIRT1, with noticeably stronger SIRT1 immunoreactivity in nuclei of primary oocytes (Fig. 3, A, D, and E). This increasing SIRT1 oocyte nuclear immunoreactivity is inverse to the decreasing NADH intensity and free/bound NADH ratios observed during the transition from primordial to primary follicles (Fig. 2).
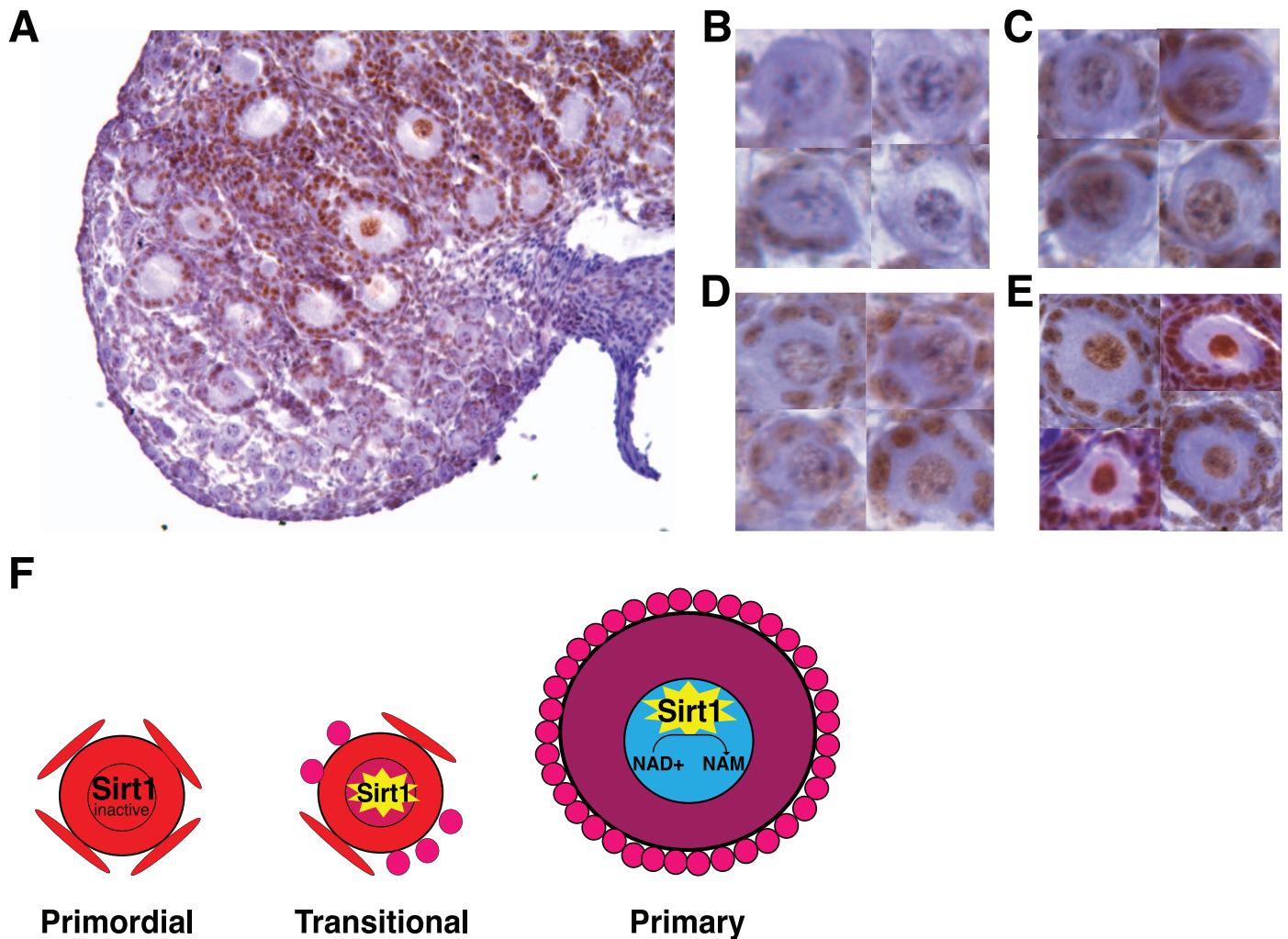
FIG. 3. SIRT1 immunostaining over the course of early stages of folliculogenesis in PND 7–9 neonatal ovary. **A**) ×20 magnification image of PND 7 neonatal ovary anti-SIRT1 immunostaining. **B**) Images of primordial follicles with oocyte nuclei immunonegative for SIRT1. **C**) Images of primordial follicles immunopositive for SIRT1. **D**) Images of transitional follicles with oocyte nuclei immunopositive for SIRT1. **E**) Images of primary follicles with oocyte nuclei strongly immunopositive for SIRT1. **F**) Proposed model for SIRT1 activity and oocyte nucleus NADH intensity depletion during the course of primordial follicle awakening. Cells are colored to indicate free/bound NADH ratio according to the color code in Figure 1C.

Changes in Free/Bound NADH During Gonadotropin-Dependent Stages of Folliculogenesis

To characterize changes in free/bound NADH during later stages of folliculogenesis, we used whole intact ovaries from prepubertal gonadotropin-stimulated female mice enriched for late secondary, antral, and preovulatory follicles (Figs. 4 and 5). Separate masking of oocyte, cumulus, and mural granulosa cell compartments allowed us to quantify free/bound NADH ratios for each compartment in antral through preovulatory staged follicles. We masked granulosa cells from secondary follicles as a single compartment.

All phasor FLIM images of PND 23 gonadotropin-stimulated secondary through preovulatory oocytes are displayed with primarily light blue pixels representative of more bound NADH (Fig. 4). Quantification of free/bound NADH in follicle compartments across follicle stages allowed us to draw multiple comparisons. We found that secondary follicle oocytes and granulosa cells 48 h post-eCG had significantly lower free/bound NADH in granulosa cells and oocytes compared to secondary follicles 7–9 h post-hCG (Fig. 5, A and D). We also observed that secondary follicle granulosa cells 48 h post-eCG have significantly lower free/bound NADH ratios than antral and preovulatory follicle cumulus granulosa cells 48 h post-eCG (Fig. 5A). Preovulatory follicle mural granulosa cells 7–9 h post-hCG displayed significantly lower free/bound NADH than secondary follicle granulosa cells 7–9 h post-hCG (Fig. 5B). Preovulatory follicle mural granulosa cells 7–9 h post-hCG had significantly higher free/bound NADH compared with preovulatory follicle mural granulosa cells 48 h post-eCG (Fig. 5B). Preovulatory oocytes 7–9 h post-hCG had significantly higher free/bound NADH compared with secondary and antral oocytes 48 h post-eCG (Fig. 5, D and E).

We also compared free/bound NADH in cumulus versus mural granulosa cell subpopulations in antral and preovulatory follicles. Mural granulosa cells had significantly lower free/bound NADH compared to cumulus granulosa cells ($P <$ 0.001, effect of granulosa cell type; Fig. 5C). However, the difference between mural granulosa cells and cumulus cells was greater in antral follicles and preovulatory follicles imaged 48 h post-eCG than in preovulatory follicles imaged 7–9 h post-hCG ($P < 0.001$, interaction between follicle group and granulosa cell type; Fig. 5C).

Although the measurements were not made in the same ovaries and the ages and gonadotropin treatment of the mice
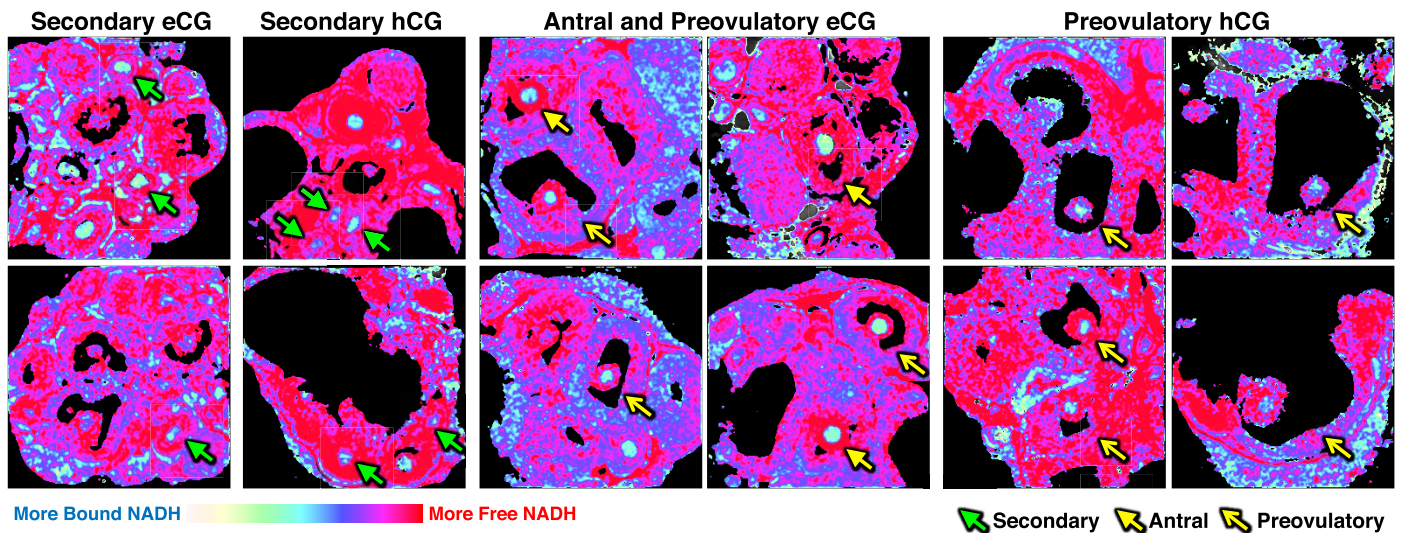
Article 129

FIG. 4. Spatial NADH intensity and lifetime dynamics over the course of secondary through preovulatory stages of folliculogenesis. Phasor FLIM images of secondary (green closed arrows), antral (yellow closed arrows), and preovulatory (yellow open arrows) follicles imaged within ovaries dissected from females after eCG or eCG+hCG stimulation starting on PND 23, as described in *Materials and Methods*; 925-μm field of view for all images. Minimal thresholding of low-intensity pixels applied to clarify follicle structures and remove background pixels in follicle antrum.

from which ovaries were collected differed, it is interesting to note that oocytes from secondary, antral, and preovulatory follicles in prepubertal gonadotropin-stimulated ovaries (Figs. 5 and 6) had lower free/bound NADH ratios compared to primordial through primary oocytes in neonatal ovaries (Figs. 2 and 6).

DISCUSSION

We applied phasor FLIM with deep-tissue imaging to discern the free/bound NADH ratio of primordial through preovulatory follicles maintained within the native biological niche of freshly dissected ex vivo ovary. This technology also enabled us to observe free/bound NADH dynamics occurring within individual follicle subcompartments without disrupting normal cellular contacts or structural integrity of the follicle during measurement. This is the first study to quantify the free/bound NADH ratio of follicles within intact ovary and also the first study to quantify this ratio separately for granulosa cells, oocyte nucleus, and oocyte cytoplasm of individual follicles. Previous work has suggested the free/bound NADH ratio mimics the ratio of intracellular NADH/NAD+ [17, 20, 23]. Accordingly, this study approximates the changes in NADH/NAD+ that occur in multiple follicular compartments during the course of folliculogenesis.

Primordial Through Primary Follicle Metabolism

Previous studies using phasor FLIM have established that the cytoplasmic free/bound NADH ratio may be utilized to infer metabolism when paired with the appropriate glycolysis and oxidative phosphorylation inhibition controls for interpretation [21–26]. Previous work has also linked changes in metabolism measured by oxygen consumption rate/extracellular acidification rate (OCR/ECAR) with changes in phasor FLIM [38]. Responses to glycolysis and oxidative phosphorylation inhibitors observed in the present study in both HeLa cells and ovarian tissue serve as further validation of phasor FLIM as a reliable means of quantifying the free/bound NADH ratio and allow us to infer interpretations about follicle metabolism (Supplemental Figures S2 and S3). All regions of

interest quantified from fresh tissue mapped within the linear combination of pure free and bound NADH lifetimes on the phasor plot, further validating the specificity of our measurements (Supplemental Figure S4).

Our data show that primordial through primary staged oocytes undergo a primarily NADH-producing metabolism with glycolysis and the Krebs cycle pathways likely the main contributors. These interpretations are based on high oocyte cytoplasm free/bound NADH ratios measured in fresh tissue as well as decreases in free/bound NADH in response to the glycolysis inhibitors 2-DG and Na DCA in cultured ovaries. We also visually observed that the cytoplasm of primordial through primary staged oocytes, as well as the granulosa and interstitial cells, are largely colored with red pixels representative of increased free NADH in phasor FLIM images. We hypothesize that NADH in the oocyte is produced through the Krebs cycle inside the mitochondrial matrix in the absence of oxidative phosphorylation because we observed no statistically significant increases in free/bound NADH when ovaries were treated with the oxidative phosphorylation inhibitor KCN. However, we observed significant decreases in free NADH in KCN-treated ovaries. We believe that inhibition of cytochrome c oxidase by KCN may impair mitochondria from optimally executing the Krebs cycle, thus decreasing free NADH. These data are consistent with a previous report suggesting that glycolysis and the Krebs cycle are important pathways in PND 1-4 primordial follicles [14]. The Krebs cycle is surmised to be a critical metabolic pathway in oocytes based on reports that denuded oocytes efficiently take up and metabolize pyruvate but have little to no ability to take up and metabolize glucose from media to produce CO_2 [14, 53, 54]. Visually, we observed more pronounced shifts toward bound NADH in granulosa and interstitial cell cytoplasm compared to oocyte cytoplasm after 2-DG or Na DCA treatment (Supplemental Figure S2, A and C). One possible explanation for this finding is that granulosa cells rely heavily on glucose and glycolysis for metabolism, while oocytes continue Krebs cycling using alternate sources of acetyl-coA derived from other pathways, such as β-oxidation [55–58].

Interestingly, the free/bound NADH ratio changed in concert with the cytoplasmic ratio in response to inhibitors
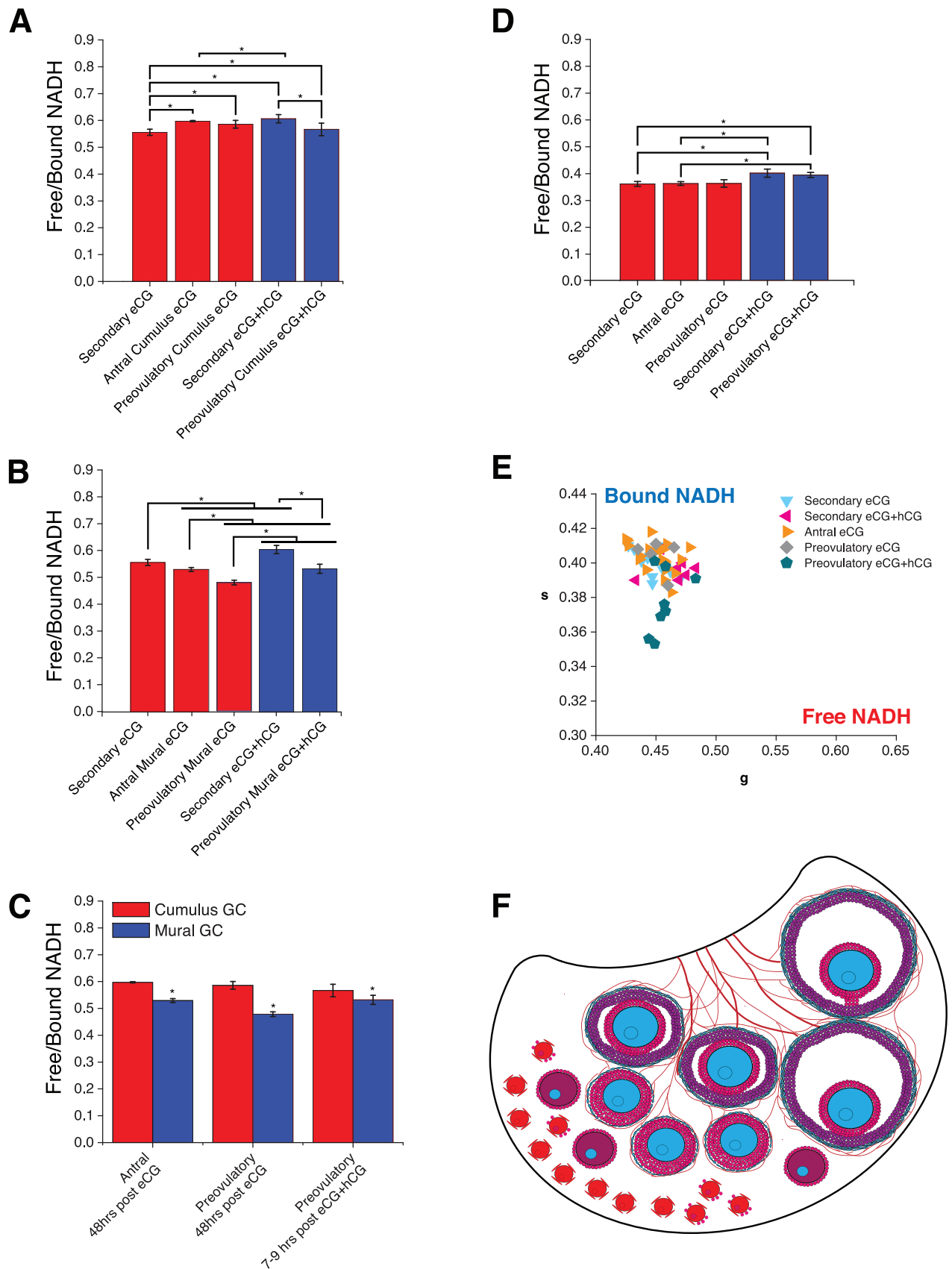
FIG. 5. Free/bound NADH in oocytes and granulosa cell subpopulations over the course of secondary through preovulatory stages of folliculogenesis. Measurements were made 48 h post-eCG or 7–9 h post-hCG administration. **A**) Mean ± SEM free/bound NADH pixels for PND 23 secondary granulosa cells, antral cumulus granulosa cells, and preovulatory cumulus granulosa ($P < 0.001$, effect of group; *$P < 0.05$ for indicated intergroup comparisons). **B**) Mean ± SEM free/bound NADH pixels for PND 23 secondary granulosa cells, antral mural granulosa cells, and preovulatory mural granulosa ($P < 0.001$, effect of group; *$P < 0.05$ for indicated intergroup comparisons). **C**) Mean ± SEM free/bound NADH in mural compared to cumulus granulosa cells for
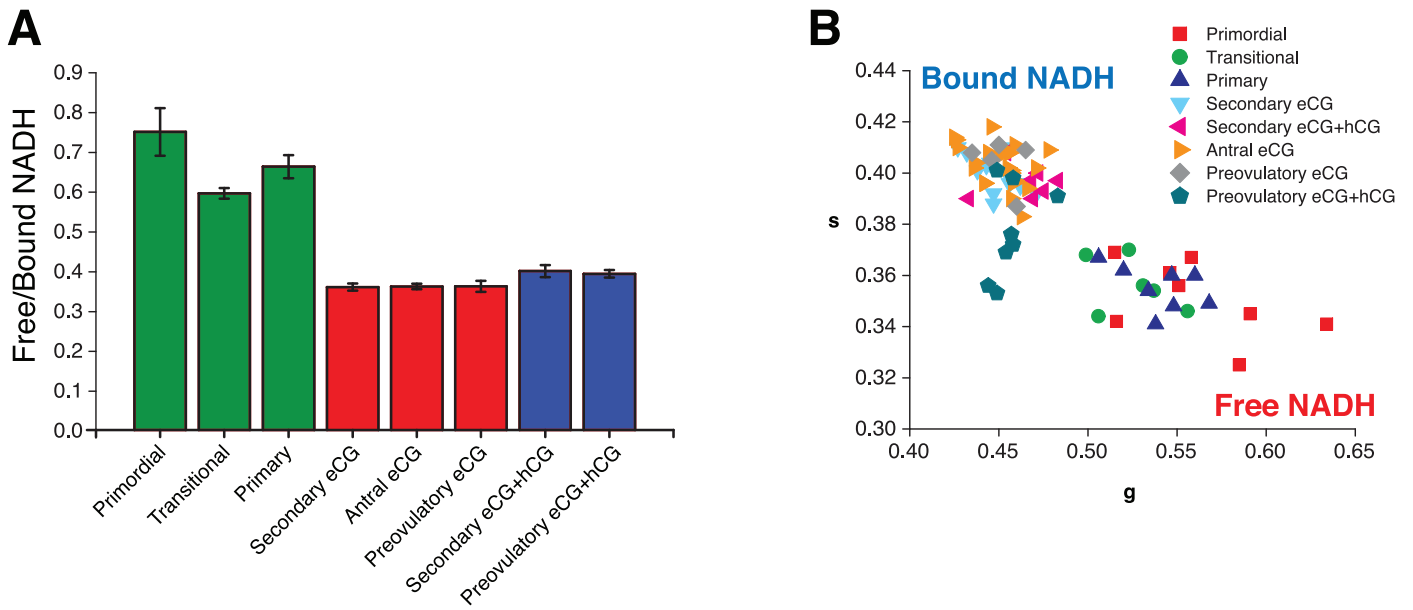
FIG. 6. Comparison of free/bound NADH ratio in the oocytes of follicles of different developmental stages in prepubertal gonadotropin-stimulated ovaries and neonatal ovaries. Oocyte free/bound NADH ratio data from Figures 2 and 5 are organized according to the type of follicle and condition of the measurement (neonatal ovary for primordial, transitional, and primary follicles and eCG or eCG+hCG stimulated prepubertal ovaries for secondary, antral, and preovulatory follicles). Free to bound NADH ratio (**A**) and position of the average of the data (**B**) in the phasor plot.

(Supplemental Figures S2 and S3). These data suggest that alterations in oocyte metabolism can impact nuclear levels of NADH and consequently have effects on oocyte nuclear maturation and nuclear NADH/NAD+-dependent regulation and signaling.

Changes in Oocyte Nuclear Free/Bound NADH and SIRT1 Expression Accompany Primordial Follicle Activation

We identified statistically significant decreases in oocyte nucleus free/bound NADH that accompany the activation of primordial follicles to the transitional/primary stages. Two main mechanisms could explain the decline in nuclear free/bound NADH, altered activities of NAD+-dependent enzymes, and exchange between the cytoplasmic and nuclear pools of NADH/NAD+. The former includes nuclear sirtuins such as SIRT1 and SIRT2 and ADP-ribosyltransferases [59]. Regarding the latter, the nuclear and cytoplasmic pools are believed to be exchangeable [59]. While all of these could be playing a role in the nuclear changes in free/bound NADH, we characterized the protein expression of SIRT1, a NAD+-dependent deacetylase. We were interested in SIRT1 due to its nuclear localization and known function to metabolize NAD+ to nicotinamide (NAM), decreasing nuclear levels of NADH [60]. SIRT1 is reportedly expressed in mouse oocytes, granulosa cells, and ovary; however, prior studies did not report on its localization in oocytes across early stages of folliculogenesis [27, 61–63]. Interestingly, we found that a subpopulation of medullary primordial follicle nuclei were immunopositive for SIRT1, whereas all oocyte nuclei of transitional and primary stage follicles were immunopositive (Fig. 3, A–E). Contrary to

previous reports, we did not observe SIRT1 in the oocyte cytoplasm [61]. We believe this could be attributed to differences in the species studied and/or in the SIRT1 antibody. The antibody we used has previously been validated in mouse tissue and has been demonstrated to have no affinity against tissue from *Sirt1−/−* mice [64]. Our SIRT1 immunostaining in PND 7–9 ovary also confirmed previous reports that SIRT1 is expressed in granulosa and interstitial cell nuclei [61, 62]. The increasing SIRT1 oocyte nuclear expression with primordial follicle awakening is intriguing, as SIRT1 is known to activate expression of PGC-1, which is involved in mitochondrial biogenesis, glucose/fatty acid metabolism, and oxidative phosphorylation [32]. The pattern of SIRT1 oocyte nuclear expression we observed was inversely related to the decreases in free/bound NADH in oocyte nuclei during the primordial to primary follicle transition (Fig. 2, A and B). These observations led us to propose a model for changes in NADH and SIRT1 expression/activity during primordial to primary oocyte maturation in which high levels of free NADH in primordial oocyte nuclei inhibit SIRT1 activity, while decreases in NADH/NAD+ that accompany primordial follicle activation release inhibition and increase nuclear activity of SIRT1, which further decreases NADH via conversion of NAD+ to NAM (Figs. 2B and 3F). This model is consistent with previous reports that SIRT1 expression and activity are inhibited by high levels of NADH [24–26]. Future studies should examine the roles of oocyte nuclear SIRT1 and NADH during primordial follicle activation.

---

antral and preovulatory follicles ($P < 0.001$, effects of GC type, follicle group, and GC type×follicle group interaction; *$P < 0.05$ compared to cumulus at same stage). **D**) Mean ± SEM free/bound NADH for PND 23 secondary, antral, and preovulatory follicle oocytes transformed from E ($P < 0.05$, effect of group; *$P < 0.05$ for indicated intergroup comparisons). **E**) Average phasor for individual secondary, antral, and preovulatory follicle oocytes plotted in g versus s; $N = 57$ follicles across nine animals. **F**) Model of free/bound NADH dynamics during primordial to preovulatory folliculogenesis in the context of the ovarian developmental niche. Cells are colored according to the color code in Figure 1C, with declining free/bound NADH from red to fuchsia to purple to blue to green. See text for details.

Late Secondary Through Preovulatory Follicle Metabolism

Overall, our observations using phasor FLIM at 740-nm two-photon excitation are consistent with previous data that whole antral and preovulatory follicles are predominantly glycolytic [12, 13, 65]. Our findings show that cumulus and mural granulosa cell metabolism is mainly glycolytic, while oocytes primarily undergo oxidative phosphorylation in these follicles.

We characterized the free/bound NADH ratio of secondary through preovulatory follicle stages in ovaries from prepubertal females injected with gonadotropins to promote follicle growth. At these stages, secondary through preovulatory oocytes have a predominantly NADH-consuming metabolism with oxidative phosphorylation likely being the main contributor. We observed mainly light blue pixels in phasor FLIM images of oocyte cytoplasm at these stages representative of low ratios of free/bound NADH compared to primordial through primary follicles (Figs. 4 and 6). These data are consistent with previous reports that have shown increased oxygen consumption in mechanically separated, pooled secondary and antral follicles [14]. We found that all populations of granulosa cells in late secondary through preovulatory follicles have predominantly NADH-producing metabolism, consistent with glycolysis/Krebs based on quantitation of free/bound NADH ratios and enrichment of red pixels in granulosa cell compartments within the follicles (Figs. 4 and 5).

Despite the overall predominantly NADH-producing metabolism in granulosa cells of secondary through preovulatory follicles, we did observe significant differences in free/bound NADH ratios between mural and cumulus granulosa cells. The mural cells had significantly lower free/bound NADH ratios, consistent with a metabolic shift toward oxidative phosphorylation compared to cumulus cells. This shift may reflect the closer proximity of mural granulosa cells to the oxygen supply provided by the capillary network within the theca cells [66]. Theca cell layers appear light green on phasor FLIM images, consistent with oxidative phosphorylation (Fig. 4). The higher ratios of free/bound NADH in cumulus compared to mural granulosa cells of antral and preovulatory follicles at 48 h post-eCG are consistent with a prior report of upregulated expression of glycolytic genes in cumulus granulosa cells compared with mural granulosa cells in PND 22 eCG-primed mouse ovaries [3].

We also observed increases in free/bound NADH in secondary oocytes, secondary granulosa cells, and preovulatory follicle mural granulosa cells in eCG+hCG-treated animals compared to eCG-treated animals. These data suggest that hCG has a stimulatory effect on NADH production or prevents NADH oxidation in these follicular cell types at these stages. This observation is consistent with previous findings that LH increased FSH-stimulated lactate production in cultured follicles matured to the preovulatory stage [12].

Limitations of the Present Study

Our study has several limitations. The phasor FLIM method provides a measure of the ratio of free/bound NADH, which previous studies suggest approximates the NADH/NAD+ ratio [17, 20, 23]. However, we cannot rule out that other factors were responsible for the differences in free/bound NADH we observed. Although the intensity images provide an indication of the relative concentrations of NADH within the tissue, we were not able to calculate the absolute concentration of NADH with the tools available to us; however, this will be possible in future studies with the availability of recently developed methods. While the ability to measure free/bound NADH ratios in freshly dissected whole, ex vivo ovaries was a strength of our study, we acknowledge that the ex vivo environment differs from the in vivo environment, and therefore one should be cautious in extrapolating our findings to the in vivo situation.

Proposed Model for Metabolism During Folliculogenesis

We propose a model for metabolic changes during follicular development based on our findings (Fig. 5F). Quiescent primordial follicles in the ovarian cortex undergo NADH-producing metabolism (glycolysis/Krebs cycle) located away from the vasculature in a hypoxic environment [6]. As follicles mature to the secondary stage, they move to the vascular ovarian medulla. As late secondary follicles mature to antral follicles, vascularization of the theca cell layer occurs [66], providing increased access to oxygen, and oocytes shift toward an NADH-consuming metabolism consistent with oxidative phosphorylation. Follicular access to increased oxygen supply promotes small increases in oxidative phosphorylation in mural granulosa cells. The oocyte relies on highly glycolytic cumulus cells as a source of pyruvate and continues oxidative phosphorylation through the preovulatory stage. From an evolutionary perspective, it would be beneficial for quiescent and early stage oocytes to use glycolysis and the Krebs cycle for energy metabolism to avoid the consequences of reactive oxygen species generated from oxidative phosphorylation and maintain primordial follicle integrity. However, oxidative phosphorylation is a much more efficient form of energy metabolism [67], and as follicular maturation progresses, so do the energy needs of the growing oocyte.

ACKNOWLEDGMENT

REFERENCES

1. Wang Z-P, Mu X-Y, Guo M, Wang Y-J, Teng Z, Mao G-P, Niu W-B, Feng L-Z, Zhao L-H, Xia G-L. Transforming growth factor-β signaling participates in the maintenance of the primordial follicle pool in the mouse ovary. J Biol Chem 2014; 289:8299–8311.
2. Tilly JL, Sinclair DA. Germline energetics, aging, and female infertility. Cell Metab 2013; 17:838–850.
3. Sugiura K, Pendola FL, Eppig JJ. Oocyte control of metabolic cooperativity between oocytes and companion granulosa cells: energy metabolism. Dev Biol 2005; 279:20–30.
4. Harris SE, Adriaens I, Leese HJ, Gosden RG, Picton HM. Carbohydrate metabolism by murine ovarian follicles and oocytes grown in vitro. Reproduction 2007; 134:415–424.
5. Collado-Fernandez E, Picton HM, Dumollard R. Metabolism throughout follicle and oocyte development in mammals. Int J Dev Biol 2012; 56:799–808.
6. Makanji Y, Tagler D, Pahnke J, Shea LD, Woodruff TK. Hypoxia-mediated carbohydrate metabolism and transport promote early-stage murine follicle growth and survival. Am J Physiol 2014; 306:E893–E903.
7. Halliwell B. Oxidative stress in cell culture: an under-appreciated problem? FEBS Lett 2003; 540:3–6.
8. Lee J-M, Mhawech-Fauceglia P, Lee N, Parsanian LC, Lin YG, Gayther SA, Lawrenson KA. A three-dimensional microenvironment alters protein expression and chemosensitivity of epithelial ovarian cancer cells in vitro. Lab Invest 2013; 93:528–542.
9. Dunning KR, Lane M, Brown HM, Yeo C, Robker RL, Russell DW.

Altered composition of the cumulus-oocyte complex matrix during *in vitro* maturation of oocytes. Hum Reprod 2007; 22:2842–2850.

10. Fernández-Gonzalez R, Moreira P, Bilbao A, Jiménez A, Pérez-Crespo M, Ramírez MA, Rodríguez De Fonseca F, Pintado B, Gutiérrez-Adán A. Long-term effect of *in vitro* culture of mouse embryos with serum on mRNA expression of imprinting genes, development, and behavior. Proc Natl Acad Sci U S A 2004; 101:5880–5885.

11. Leese HJ, Lenton EA. Glucose and lactate in human follicular fluid: concentrations and interrelationships. Hum Reprod 1990; 5:915–919.

12. Boland NI, Humpherson PG, Leese HJ, Gosden RG. Pattern of lactate production and steroidogenesis during growth and maturation of mouse ovarian follicles in vitro. Biol Reprod 1993; 48:798–806.

13. Boland NI, Humpherson PG, Leese HJ, Gosde RG. The effect of glucose metabolism on murine follicle development and steroidogenesis *in vitro*. Hum Reprod 1994; 9:617–623.

14. Harris SE, Leese HJ, Gosden RG, Picton HM. Pyruvate and oxygen consumption throughout the growth and development of murine oocytes. Mol Reprod Dev 2009; 76:231–238.

15. Lin S-J, Guarente L. Nicotinamide adenine dinueleotide, a metabolic regulator of transcription, longevity and disease. Curr Opin Cell Biol 2003; 15:241–246.

16. Heikal AA. Intracellular coenzymes as natural biomarkers for metabolic activities and mitochondrial anomalies. Biomark Med 2010; 4:241–263.

17. Stringari C, Edwards RA, Pate KT, Waterman ML, Donovan PJ, Gratton E. Metabolic trajectory of cellular differentiation in small intestine by phasor fluorescence lifetime microscopy of NADH. Sci Rep 2012; 2: 561–569.

18. Mayevsky A, Rogatsky GG. Mitochondrial function in vivo evaluated by NADH fluorescence: from animal models to human studies. Am J Physiol 2007; 292:C615–C640.

19. Mayevsky A, Chance B. Oxidation-reduction states of NADH in vivo: from animals to clinical use. Mitochondrion 2007; 7:330–339.

20. Bird DK, Yan L, Vrotsos KM, Eliceiri KW, Vaughan EM, Keely PJ, White JG, Raamanujam N. Metabolic mapping of MCF10A human breast cells via multiphoton fluorescence lifetime imaging of the coenzyme NADH. Cancer Res 2005; 65:8766–8773.

21. Kasischke KA, Vishwasrao HD, Fisher PJ, Zipfel WR, Webb WW. Neural activity triggers neuronal oxidative metabolism followed by astrocytic glycolysis. Science 2004; 305:99–103.

22. Michaelis L, Menten ML, Johnson KA, Goody RS. The original Michaelis constant: translation of the 1913 Michaelis-Menton paper. Biochemistry (Mosc) 2011; 50:8264–8269.

23. Lakowicz JR, Szmacinski H, Nowaczyk K, Johnson ML. Fluorescence lifetime imaging of free and protein-bound NADH. Proc Natl Acad Sci U S A 1992; 89:1271–1275.

24. Revollo JR, Grimm AA, Imai S-I. The NAD biosynthesis pathway mediated by nicotinamide phosphoribosyltransferase regulates Sir2 activity in mammalian cells. J Biol Chem 2004; 279:50754–50763.

25. Lin S-J, Ford E, Haigis M, Liszt G, Guarente L. Calorie restriction extends yeast life span by lowering the level of NADH. Genes Dev 2004; 18: 12–16.

26. Braidy N, Guillemin GJ, Mansour H, Chan-Ling T, Poljak A, Grant R. Age related changes in NAD+ metabolism oxidative stress and Sirt1 activity in Wistar rats. PLoS One 2011; 6:e19194.

27. Coussens M, Maresh JG, Yanagimachi R, Maeda G, Allsopp R. Sirt1 deficiency attenuates spermatogenesis and germ cell function. PLoS One 2008; 3:e1571.

28. Zhang X-M, Li L, Xu J-J, Wang N, Liu W-J, Lin X-H, Fu Y-C, Luo L-L. Rapamycin preserves the follicle pool reserve and prolongs the ovarian lifespan of female rats via modulating mTOR activation and sirtuin expression. Gene 2013; 523.

29. Motta MC, Divecha N, Lemieux M, Kamel C, Chen D, Bultsma Y, McBurney M, Guarente L. Mammalian SIRT1 represses forkhead transcription factors. Cell 2004; 116:551–563.

30. John GB, Gallardo TD, Shirley LJ, Castrillon DH. Foxo3 is a PI3K-dependent molecular switch controlling the initiation of oocyte growth. Dev Biol 2008; 321:197–204.

31. Castrillon DH, Miao L, Kollipara R, Horner JW, DePinho RA. Suppression of ovarian follicle activation in mice by the transcription factor Foxo3a. Science 2003; 301:215–218.

32. Nemoto S, Fergusson MM, Finkel T. SIRT1 functionally interacts with the metabolic regulator and transcriptional coactivator PGC-1α. J Biol Chem 2005; 280:15456–16460.

33. Rodgers JT, Lerin C, Haas W, Gygi SP, Speigelman BM, Puigserver P. Nutrient control of glucose homeostasis through a complex of PGC-1α and SIRT1. Nature 2005; 434:113–118.

34. Digman MA, Caiolfa VR, Zamai M, Gratton E. The phasor approach to fluorescence lifetime imaging analysis. Biophys J 2008; 94:L14–L16.

35. Stringari C, Cinquin A, Cinquin O, Digman MA, Donovan PJ, Gratton E. Phasor approach to fluorescence lifetime microscopy distinguishes different metabolic states of germ cells in a live tissue. Proc Natl Acad Sci U S A 2011; 108:13582–13587.

36. Datta R, Alfonso-García A, Cinco R, Gratton E. Fluorescence lifetime imaging of endogenous biomarker of oxidative stress. Sci Rep 2015; 5: 9848.

37. Wright BK, Andrews LM, Markham J, Jones MR, Stringari C, Digman MA, Gratton E. NADH distribution in live progenitor stem cells by phasor-fluorescence lifetime image microscopy. Biophys J 2012; 103: L7–L9.

38. Pate KT, Stringari C, Sprowl-Tanio S, Wang K, TeSlaa T, Hoverter NP, McQuade MM, Garner C, Digman MA, Teitell MA, Edwards RA, Gratton E, et al. Wnt signaling directs a metabolic program of glycolysis and angiogenesis in colon cancer. EMBO J 2014; 33:1454–1473.

39. Scott TG, Spencer RD, Leonard NJ, Weber G. Emission properties of NADH. Studies of fluorescence lifetimes and quantum efficiencies of NADH, AcPyADH, and simplified synthetic models. J Am Chem Soc 1970; 92:687–695.

40. Szabó P, Hübner K, Schöler H, Mann JR. Allele-specific expression of imprinted genes in mouse migratory primordial germ cells. Mech Dev 2002; 115:157–160.

41. Truett GE, Heeger P, Mynatt RL, Truett AA, Walker JA, Warman ML. Preparation of PCR-quality mouse genomic DNA with hot sodium hydroxide and Tris (HotSHOT). Biotechniques 2000; 29:52–54.

42. Crosignani V, Dvornikov AS, Gratton E. Enhancement of imaging depth in turbid media using a wide area detector. Biophotonics 2011; 4:592–599.

43. Crosignani V, Dvornikov AS, Aguilar JS, Stringari C, Edwards R, Mantulin WW, Gratton E. Deep tissue fluorescence imaging and *in vivo* biological applications. J Biomed Optics 2012; 17:116021–116028.

44. Gratton E. Globals Software for Spectroscopy (GlobalsWE) and Images (SimFCS) [Internet]. http://www.lfd.uci.edu/globals. Accessed 20 May 2011.

45. Wilkerson CWJ, Goodwin PM, Ambrose WP, Martin JC, Keller RA. Detection and lifetime measurement of single molecules in flowing sample streams by laser-induced fluorescence. Appl Phys Lett 1993; 62: 2030–2032.

46. Lopez SG, Luderer U. Effects of cyclophosphamide and buthionine sulfoximine on ovarian glutathione and apoptosis. Free Radic Biol Med 2004; 36:1366–1377.

47. Pedersen T, Peters H. Proposal for a classification of oocytes in the mouse ovary. J Reprod Fertil 1968; 17:555–557.

48. Kankotia S, Stacpoole PW. Dichloroacetate and cancer: new home for an orphan drug? Biochim Biophys Acta 2014; 1846:617–629.

49. van Waveren C, Sun Y, Cheung HS, Morales CT. Oxidative phosphor-ylation dysfunction modulates expression of extracellular matrix-remod-eling genes and invasion. Carcinogenesis 2006; 27:409–418.

50. Devin A, Guérin B, Rigoulet M. Control of oxidative phosphorylation in rat liver mitochondria: effect of ionic media. Biochim Biophys Acta 1997; 1319:293–300.

51. Michán S, Li Y, Chou MM-H, Parrella E, Ge H, Long JM, Allard JS, Lewis K, Miller M, Xu W, Mervis RF, Chen J, et al. SIRT1 is essential for normal cognitive function and synaptic plasticity. J Neurosci 2010; 30: 9695–9707.

52. Way JL. Cyanide intoxication and its mechanism of antagonism. Annu Rev Pharmacol Toxicol 1984; 24:451–481.

53. Eppig JJ. Analysis of mouse oogenesis in vitro. Oocyte isolation and the utilization of exogenous energy sources by growing oocytes. J Exp Zool 1976; 198:375–382.

54. Biggers JD, Whittingham DG, Donahue RP. The pattern of energy metabolism in the mouse oocyte and zygote. Proc Natl Acad Sci U S A 1967; 58:560–567.

55. Dunning KR, Cashman K, Russell DL, Thompson JG, Norman RJ, Robker RL. Beta-oxidation is essential for mouse oocyte developmental competence and early embryo development. Biol Reprod 2010; 83: 909–918.

56. Sturmey RG, Reis A, Leese HJ, McEvoy TG. Role of fatty acids in energy provision during oocyte maturation and early embryo development. Reprod Domest Anim 2009; 44(suppl 3):50–58.

57. Paczkowski M, Silva E, Schoolcraft WB, Krisher RL. Comparative importance of fatty acid beta-oxidation to nuclear maturation, gene expression, and glucose metabolism in mouse, bovine, and porcine cumulus oocyte complexes. Biol Reprod 2013; 88:111.

58. Gu L, Liu H, Gu X, Boots C, Moley KH, Wang Q. Metabolic control of

Article 129

oocyte development: linking maternal nutrition and reproductive outcomes. Cell Mol Life Sci 2015; 72:251–271.

59. Koch-Nolte F, Fischer S, Haag F, Ziegler M. Compartmentation of NAD$^+$-dependent signaling. FEBS Lett 2011; 585:1651–1656.

60. Cantó C, Auwerx J. Targeting sirtuin 1 to improve metabolism: all you need is NAD+? Pharmacol Rev 2012; 64:166–187.

61. Luo L-L, Chen X-C, Fu Y-C, Xu J-J, Li L, Lin X-H, Xiang YF, Zhang X-M. The effects of caloric restriction and a high fat diet on ovarian lifespan and the expression of SIRT1 and SIRT6 proteins in rats. Aging Clin Exp Res 2012; 24:125–133.

62. Di Emidio G, Falone S, Vitti M, D'Alessandro AM, Vento M, Di Pietro C, Amicarelli F, Tatone C. SIRT1 signalling protects mouse oocytes against oxidative stress and is deregulated during aging. Hum Reprod 2014; 29: 2006–2017.

63. Tatone C, Di Emidio G, Vitti M, Di Carlo M, Santini SJ, D'Alessandro AM, Falone S, Amicarelli F. Sirtuin functions in female fertility: possible role in oxidative stress and aging. Oxid Med Cell Longev 2015; 2015: 1–11.

64. Boily G, He XH, Pearce B, Jardine K, McBurney MW. SirT1-null mice develop tumors at normal rates but are poorly protected by resveratrol. Oncogene 2009; 28:2882–2893.

65. Boland NI, Humpherson PG, Leese HJ, Gosden RG. Characterization of follicular energy metabolism. Hum Reprod 1994; 9:604–609.

66. Brown HM, Russell DL. Blood and lymphatic vasculature in the ovary: development, function, and disease. Hum Reprod Update 2014; 20:29–39.

67. Zheng J. Energy metabolism of cancer: glycolysis versus oxidative phosphorylation (review). Oncol Lett 2012; 4:1151–1157.